frontiers | Frontiers in Nanotechnology

TYPE Original Research
PUBLISHED 29 August 2025
DOI 10.3389/fnano.2025.1632279

OPEN ACCESS

EDITED BY
Trupti Ranjan Lenka,
National Institute of Technology, Silchar, India

REVIEWED BY
Gayani K. Nandasiri,
University of Moratuwa, Sri Lanka
Raghunandan Swain,
Parala Maharaja Engineering College (P.M.E.C), India

*CORRESPONDENCE
Jong-Hoon Kim,
jh.kim@wsu.edu

RECEIVED 20 May 2025
ACCEPTED 07 August 2025
PUBLISHED 29 August 2025

CITATION
Khan AA, Ban S, Yeo W-H and Kim J-H (2025) A comparative study of flexible electrode design on the performance of flexible wearable electronics.
Front. Nanotechnol. 7:1632279.
doi: 10.3389/fnano.2025.1632279

A comparative study of flexible electrode design on the performance of flexible wearable electronics

Akib Abdullah Khan[1], Seunghyeb Ban[2], Woon-Hong Yeo[2,3,4] and Jong-Hoon Kim[1,5]*

[1]School of Engineering and Computer Science, Washington State University, Vancouver, WA, United States, [2]George W. Woodruff School of Mechanical Engineering, Georgia Institute of Technology, Atlanta, GA, United States, [3]Wearable Intelligent Systems and Healthcare Center (WISH Center) at the Institute for Matter and Systems, Georgia Institute of Technology, Atlanta, GA, United States, [4]Wallace H. Coulter Department of Biomedical Engineering, Georgia Tech and Emory University School of Medicine, Atlanta, GA, United States, [5]Department of Mechanical Engineering, University of Washington, Seattle, WA, United States

Flexible wearable electronics are promising for continuous health monitoring, particularly in electromyography (EMG) applications. A critical factor in their performance is electrode design, which affects mechanical resilience and electrical stability. Here, this study develops multiple electrode geometries: open-mesh, closed-mesh, and island-bridge, fabricated from gold-coated polyimide substrates to offer the best performance in EMG detection. Under standardized bending and stretching tests, the island-bridge design shows the lowest resistance variation (±1.61%), while the closed-mesh design provides balanced performance across various strains. EMG tests indicate that the closed-mesh electrodes deliver the highest signal-to-noise ratios (up to 14.83 dB) with minimal motion artifacts. Although the open-mesh design is flexible, it has lower electrical stability. In summary, the closed-mesh performs best overall, the open-mesh is better for handling motion artifacts, and the island-bridge is ideal for areas with minimal movement.

KEYWORDS

flexible electronics, electrode design, health monitoring, wearable electronics, electromyography

1 Introduction

Flexible electronics have revolutionized the development of wearable and implantable technologies by enabling lightweight, bendable, and conformal devices that can integrate seamlessly with the human body. These systems are increasingly used in applications such as smart textiles, health monitoring, and soft robotics, where conventional rigid electronics fall short due to mechanical mismatch and lack of adaptability (Lee et al., 2021; Wen and Fang, 2022; Abbas et al., 2024). A critical component in these systems is the electrode, which serves as the primary interface for signal acquisition, power delivery, or sensing.

The mechanical and electrical performance of flexible electronics is heavily influenced by the design of the electrodes. Geometry determines how mechanical strain is distributed across the substrate and affects both durability and signal fidelity. Designs such as serpentine, wrinkled, and mesh-based patterns have been shown to improve stretchability, reduce localized stress, and enhance conformal contact with skin

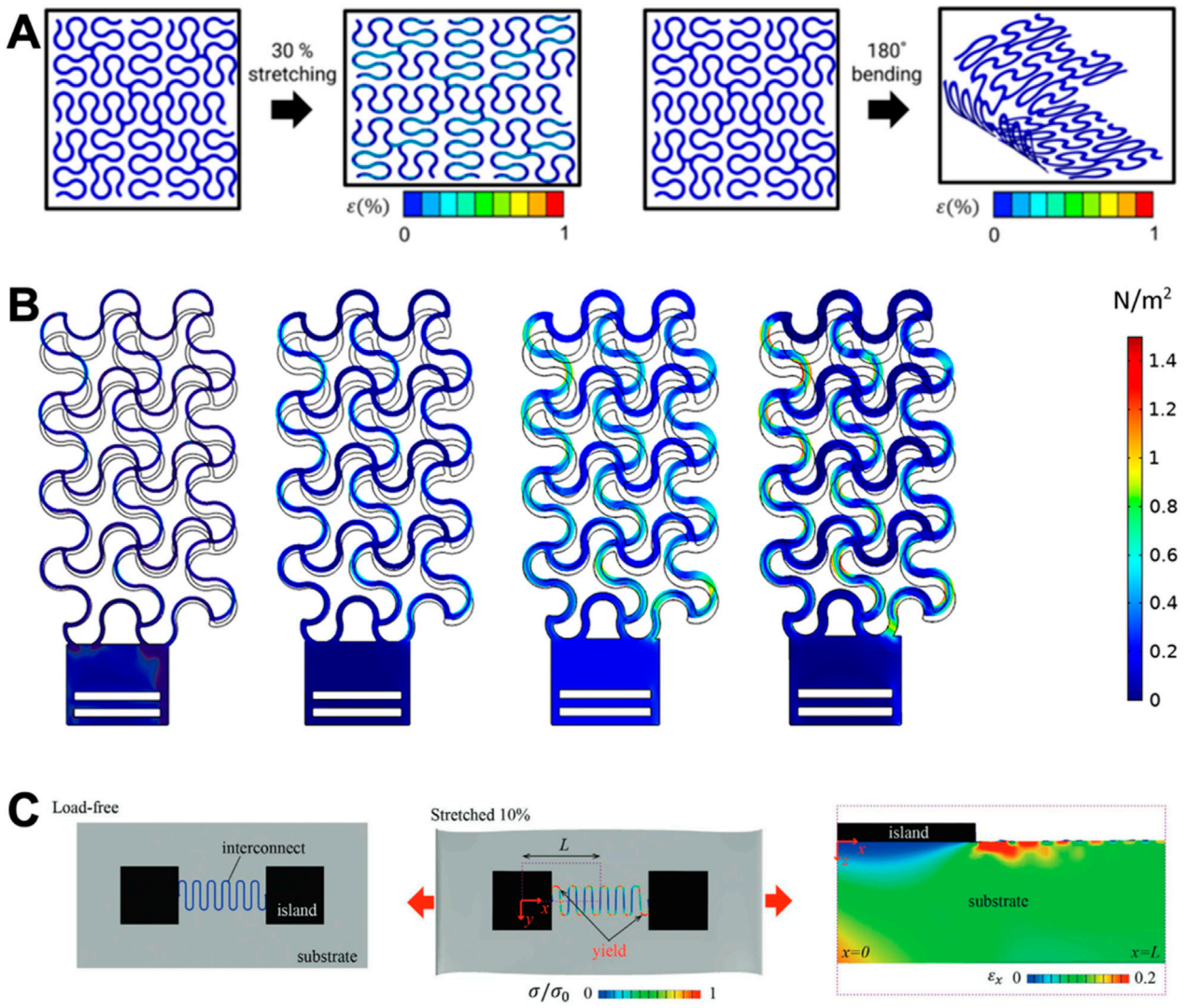

FIGURE 1
Finite element analysis (FEA) simulation results from the literature illustrating strain distribution in three flexible electrode geometries under mechanical deformation: **(A)** open-mesh, **(B)** closed-mesh, and **(C)** island-bridge. These published simulations demonstrate how each design manages mechanical stress, highlighting differences in strain localization and structural resilience.

(Sakamoto et al., 2018; Cheng et al., 2023a). For instance, serpentine traces redistribute strain more evenly, while microstructured or ultra-thin substrates promote out-of-plane buckling to absorb deformation without fracturing (Pan et al., 2017; Xu et al., 2023). These advances have made it possible to achieve strains exceeding 30%–40% while maintaining electrical integrity.

Among various approaches, three geometrical strategies have gained prominence in the literature: open-mesh, closed-mesh, and island-bridge designs. The open-mesh design, which incorporates serpentine traces with large open spaces, maximizes stretchability and is ideal for applications that require extensive deformation or surface conformity (Wang et al., 2020; Park et al., 2023; Wang et al., 2020; Park et al., 2023). However, this comes at the cost of increased resistance and reduced functional coverage due to longer current paths and sparse material distribution (Hocheng and Chen, 2014). The closed-mesh design strikes a balance between flexibility and electrical stability by forming a denser network of conductive traces, which supports reliable performance during moderate strain (Eyvazi Hesar et al., 2021a). Finally, the island-bridge architecture utilizes rigid electrode islands connected by soft, stretchable bridges, which localize mechanical deformation away from sensitive regions. This design is highly effective in decoupling mechanical and electrical strain, but may suffer from strain concentration near the bridges and higher fabrication complexity (Li and Liu, 2019; Silva et al., 2020; Yin et al., 2020).

Representative FEA simulations from the literature are shown in Figures 1A–C, illustrating the mechanical response of each design. Figure 1A (Park et al., 2023) shows that the open-mesh design effectively redistributes strain along serpentine paths, minimizing stress concentration but experiencing strain near corners. Figure 1B (Eyvazi Hesar et al., 2021b) demonstrates the uniform strain distribution in a closed-mesh structure due to its compact conductive network, resulting in improved resilience under tension. Figure 1C (Li et al., 2022) reveals strain localization near

TABLE 1 Design parameters of the flexible wearable electrodes.

Parameter	Value/Description
Electrode Types	Open-mesh, Closed-mesh, Island-type
Design Method	CAD software
Conductive Path Area Ratio	~0.5 (conductive path area/total electrode area)
Symmetry	Symmetrical along both longitudinal and transverse axes
Trace Width	0.8 mm
Electrode Dimensions	11.21 mm × 11.21 mm
Minimum Gap Between Paths	0.21 mm
Reference for Illustrations	Figures 3A–C

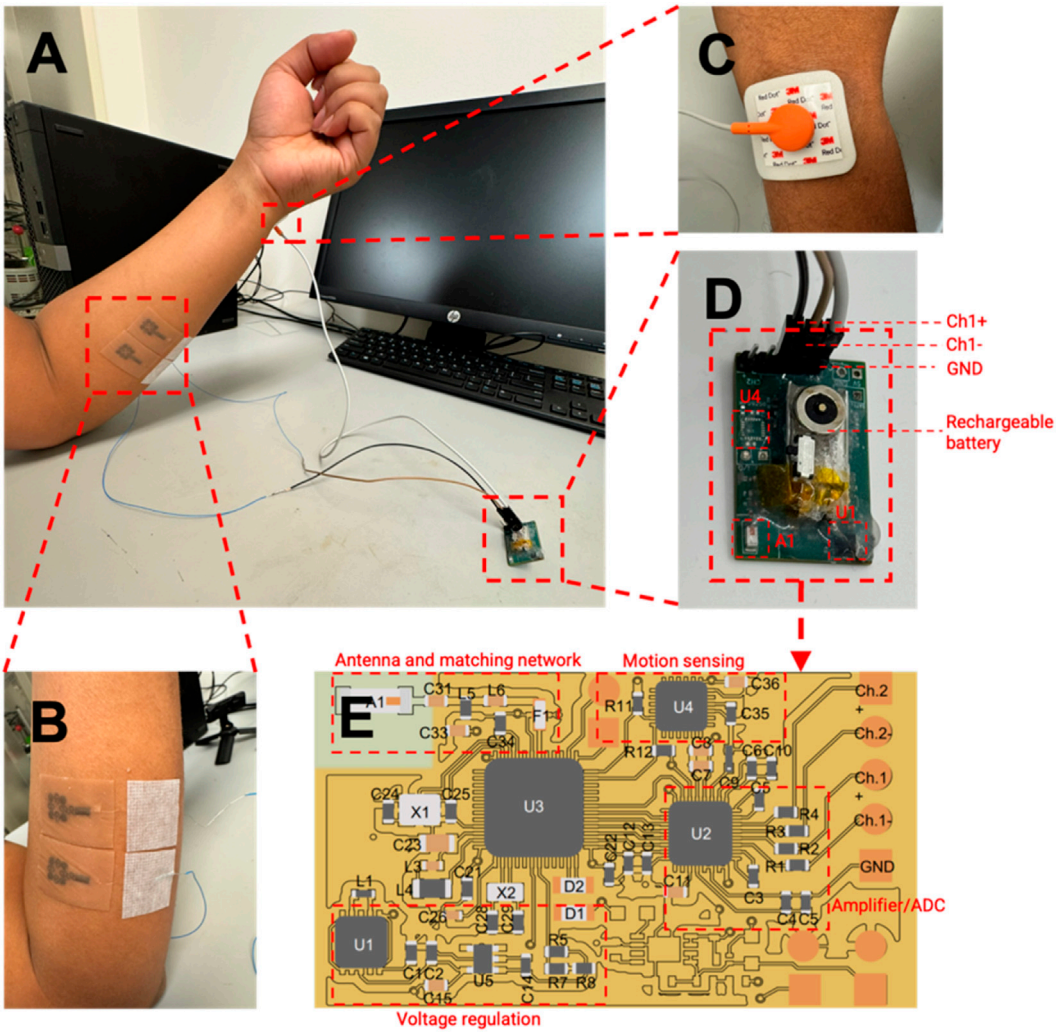

FIGURE 2
Experimental setup for EMG signal acquisition. **(A)** Placement of flexible electrodes and commercial gel reference on the forearm, **(B)** Enlarged view of a flexible measurement electrode. **(C)** Commercial gel reference electrode (3M Red Dot). **(D)** Custom Bluetooth Low Energy (BLE) circuit with antenna and battery. **(E)** Block diagram of BLE circuit components used for EMG data collection and transmission (Kwon et al., 2020).

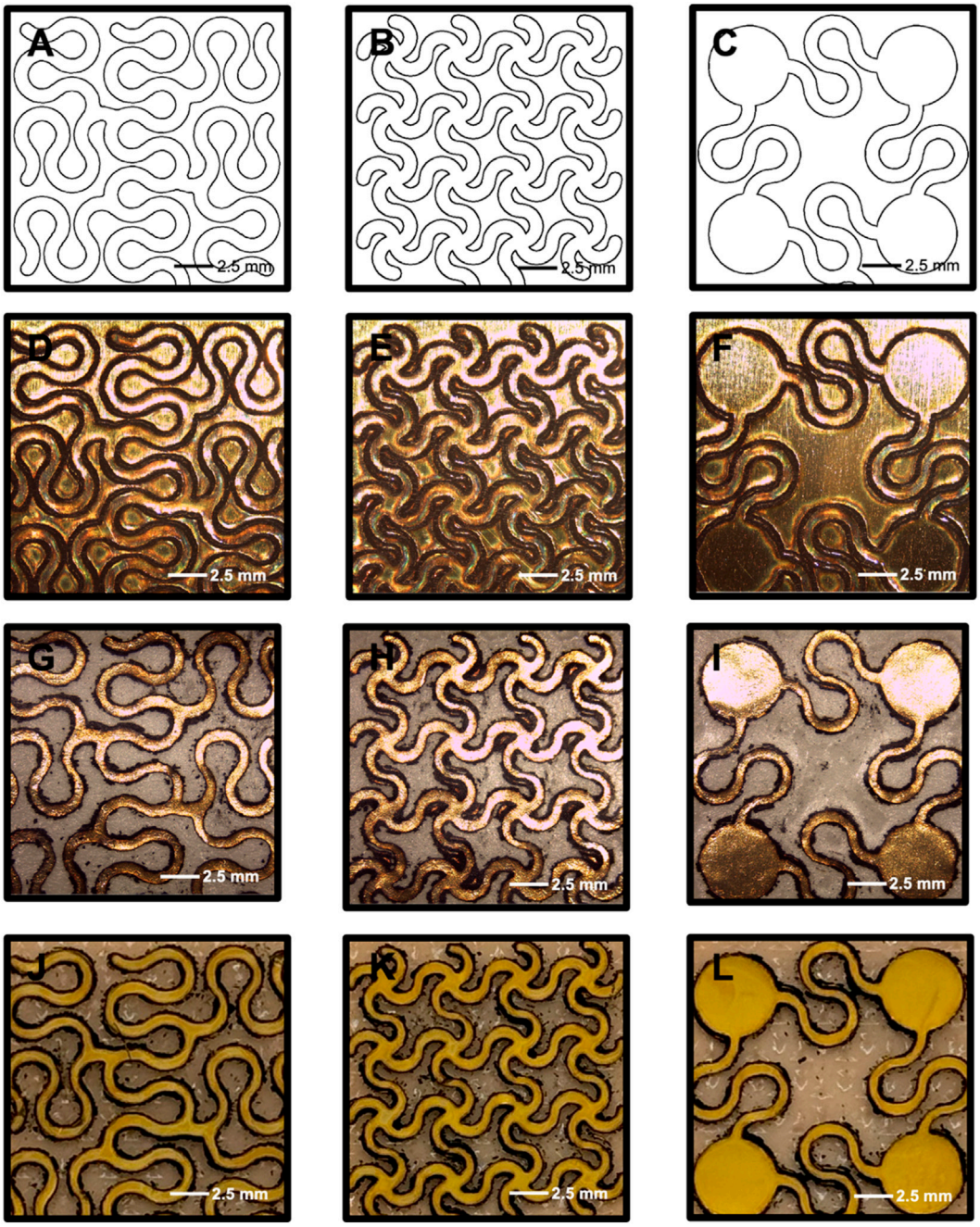

FIGURE 3
Fabrication process and final forms of the three electrode designs. **(A–C)** CAD designs of the open-mesh, closed-mesh, and island-bridge patterns. **(D–F)** Laser-cut gold-coated PI electrodes on glass/PDMS substrate. **(G–I)** Electrodes transferred to water-soluble tape. **(J–L)** Final electrode assemblies on silicone backing, ready for use.

the bridges of the island-bridge design, attributed to the modulus mismatch between stiff islands and soft connectors.

Despite the progress in flexible electrode designs, comparative studies are often limited by inconsistencies in material selection, fabrication techniques, or electrode area, which introduce confounding factors and hinder objective evaluation. To our knowledge, no prior study has systematically compared these three commonly used geometries—open-mesh, closed-mesh, and island-bridge—under identical material, fabrication, and testing conditions. This gap makes it difficult to isolate the role of geometry in determining mechanical resilience and signal quality in wearable applications.

In this study, we address this gap by conducting a controlled comparative analysis of open-mesh, closed-mesh, and island-bridge electrodes. All designs were fabricated using a standardized process, including gold-coated polyimide (PI) substrates, chromium adhesion layers, and optimized laser cutting parameters. To ensure a fair comparison, the total conductive area and trace

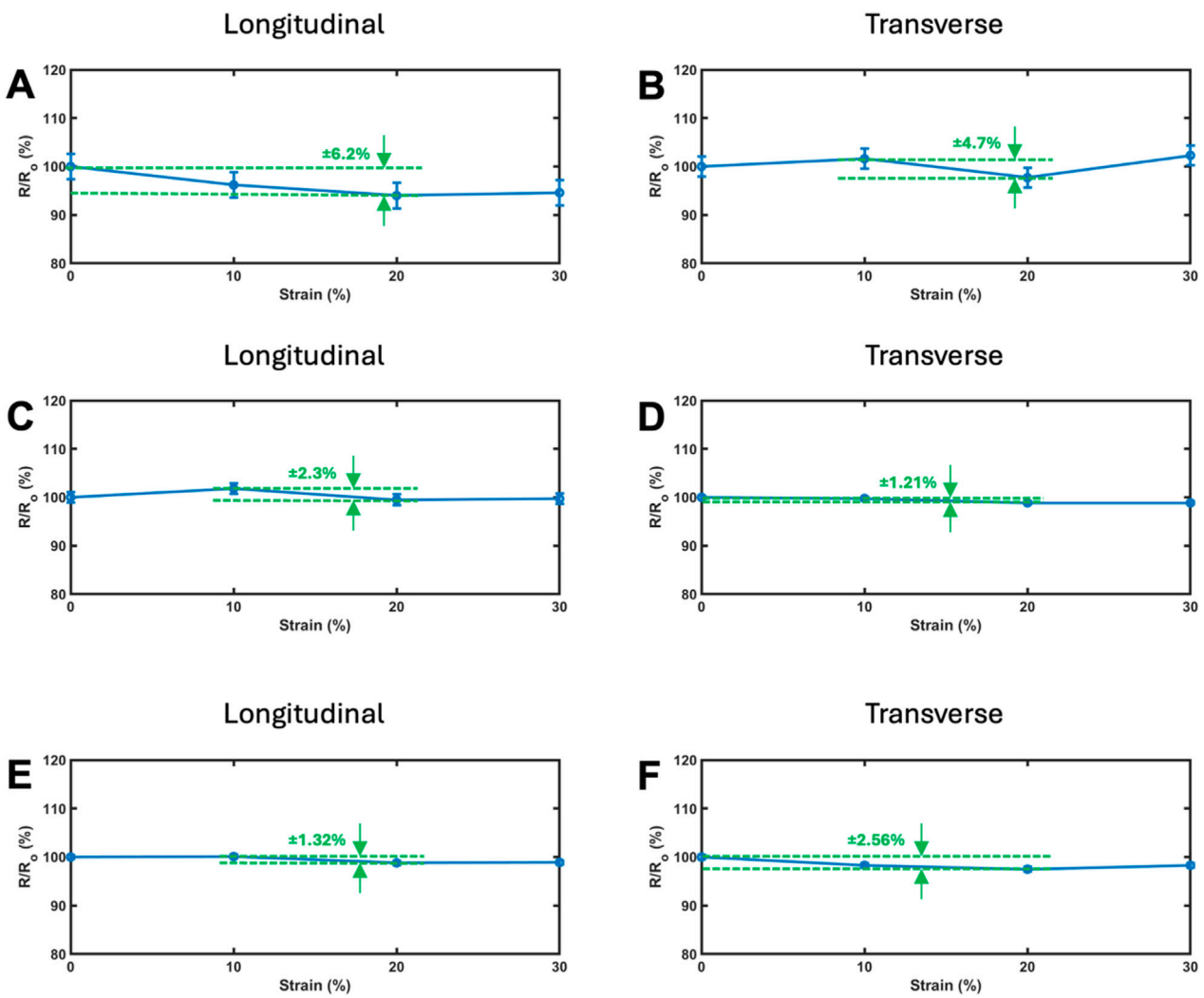

FIGURE 4
Relative resistance change ($\Delta R/R_0$) as a function of uniaxial strain (0%–30%) for the three electrode designs under longitudinal and transverse stretching. **(A,B)** Open-mesh electrode under **(A)** longitudinal and **(B)** transverse strain. **(C,D)** Closed-mesh electrode under **(C)** longitudinal and **(D)** transverse strain. **(E,F)** Island-bridge electrode under **(E)** longitudinal and **(F)** transverse strain. The closed-mesh and island-bridge designs exhibit lower resistance variation across both directions, indicating superior electromechanical stability compared to the open-mesh design.

TABLE 2 Maximum resistance variation ($\Delta R/R_0$) observed in each electrode design under uniaxial stretching. Results are reported for both longitudinal and transverse strain directions up to 30% strain. The values reflect electromechanical stability across the open-mesh, closed-mesh, and island-bridge geometries.

Stretching Direction	Maximum resistance variation (%)		
	Open-Mesh Design	Closed-Mesh Design	Island-Bridge Design
Longitudinal	±6.2	±2.3	±1.32
Transverse	±4.7	±1.21	±2.56

width were kept consistent across all patterns. Mechanical reliability was evaluated through cyclic bending and uniaxial stretching tests, and real-time EMG signals were acquired using a Bluetooth Low Energy (BLE)-based circuit during various motion tasks. Signal quality was assessed using signal-to-noise ratio (SNR) metrics, and deformation effects were studied under both folding and twisting conditions.

By minimizing variability in materials and processing, this study enables a direct assessment of how electrode geometry alone influences key performance indicators such as mechanical

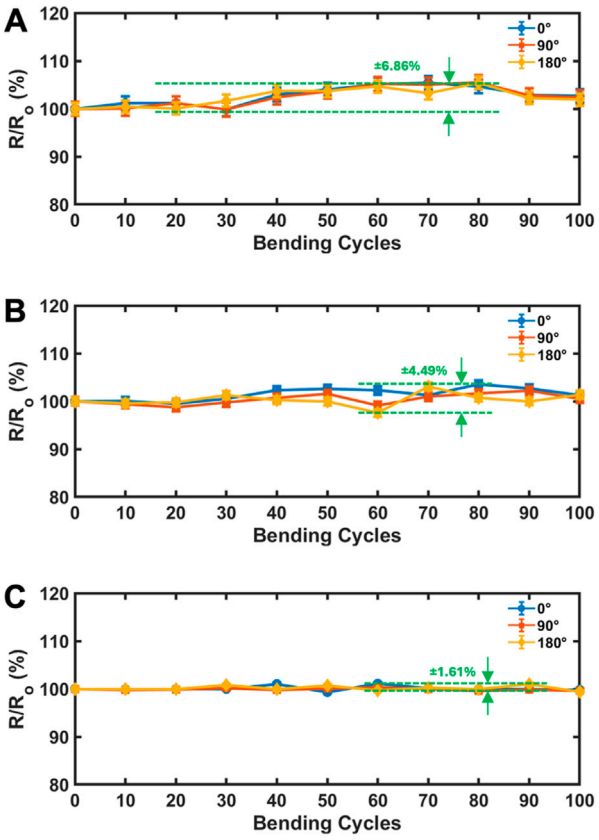

FIGURE 5
Relative resistance of printed electrodes measured during cyclic bending tests, showing negligible change over repeated cycles for **(A)** open-mesh, **(B)** closed-mesh, and **(C)** island-bridge designs, indicating stable electrical performance under mechanical deformation. The island-bridge design shows the most stable electrical behavior, while the open-mesh design demonstrates the largest resistance drift due to structural fatigue.

durability, stretchability, and bioelectrical signal fidelity. The results offer actionable guidance for optimizing electrode design in next-generation flexible and wearable electronics.

2 Materials and methods

2.1 Electrode designs

Three conventional electrode patterns—open-mesh, closed-mesh, and island-bridge—were designed using CAD software. To ensure a consistent basis for comparison, key geometric parameters such as area density, trace width, gap size, and symmetry were standardized across all designs. Specifically, the conductive path area was maintained at approximately 50% of the total electrode area for each pattern. All designs featured symmetrical layouts along both the longitudinal and transverse axes, with a uniform trace width of 0.8 mm. The overall electrode dimensions were fixed at 11.21 mm × 11.21 mm, and the minimum spacing between adjacent conductive paths was set to 0.21 mm. The design parameters are also listed in Table 1.

TABLE 3 Average signal-to-noise ratio (SNR) values obtained during EMG signal acquisition under three types of hand motions—folding, counterclockwise twisting, and clockwise twisting. SNR is reported (mean ± standard deviation) for each of the three electrode designs, highlighting the influence of geometry on signal quality during dynamic movement.

Motion Type	Signal-to-noise ratio (dB)		
	Open-Mesh Design	Motion Type	Open-Mesh Design
Motion Type	Open-Mesh Design	Motion Type	Open-Mesh Design
Folding	9.67 ± 1.13	12.66 ± 2.53	10.34 ± 4.74
Twist CCW	9.07 ± 0.37	11.78 ± 0.53	10.31 ± 4.7
Twist CW	9.34 ± 1.01	14.83 ± 1.94	13.99 ± 7.18

2.2 Substrate preparation

PI film (3M Polyimide Film Tape 5,413, 69 μm thick) was selected as the flexible substrate for this study. To facilitate precise laser cutting, the polyimide (PI) film was temporarily bonded to glass slides using polydimethylsiloxane (PDMS) as a reversible adhesive layer. The glass support provided a rigid, flat backing necessary to stabilize the flexible polyimide film during sputtering and laser cutting, ensuring uniform processing and preventing deformation. PDMS was chosen for its ability to provide strong temporary adhesion during fabrication processes (including sputtering and laser cutting) while allowing clean removal of the PI film without significant residue - a critical requirement for maintaining substrate integrity in flexible electronics applications (Borók et al., 2021; Jiang et al., 2022). The process began with the preparation of a five″ x 4″ glass slide. Before spin-coating, the PDMS base (DOWSIL 184 Silicon Elastomer Base) was mixed with its curing agent (DOWSIL 184 Silicone Elastomer Curing Agent) in a 10:1 ratio (Shamsiah Mohamed and Ching Theng, 2019; Kim et al., 2021). The thickness of the PDMS film was around 20–25 μm (Lee et al., 2006). The mixture was then degassed using a vacuum desiccator to eliminate air bubbles. The glass slide was prebaked at 120 °C for 90 s to ensure a clean and dry surface. The PDMS mixture was spin-coated onto the glass slide in two steps: first at 500 rpm for 10 s, followed by a second step at 5,000 rpm for 30 s. After spin-coating, the PDMS layer was cured at 100 °C for 1 h. Once the PDMS layer was fully cured, the polyimide film was aligned and gently laminated onto the surface of the glass slide using uniform manual pressure to ensure full contact without trapping air bubbles. This prepared substrate was then ready for the deposition of the conductive layer.

2.3 Conductive layer deposition

Gold was selected as the conductive layer for the flexible wearable sensor. A 30 nm layer of gold was sputtered onto the PI film. To address the poor adhesion of gold to PI, a thin 5 nm layer of chromium was first sputtered between the gold and PI layers (Schneider et al., 2003; Todeschini et al., 2017). The sputtering process was carried out using a Nano36 sputter, which employs magnetron sputtering. The sputtering rates were set at 0.3 Å/s for

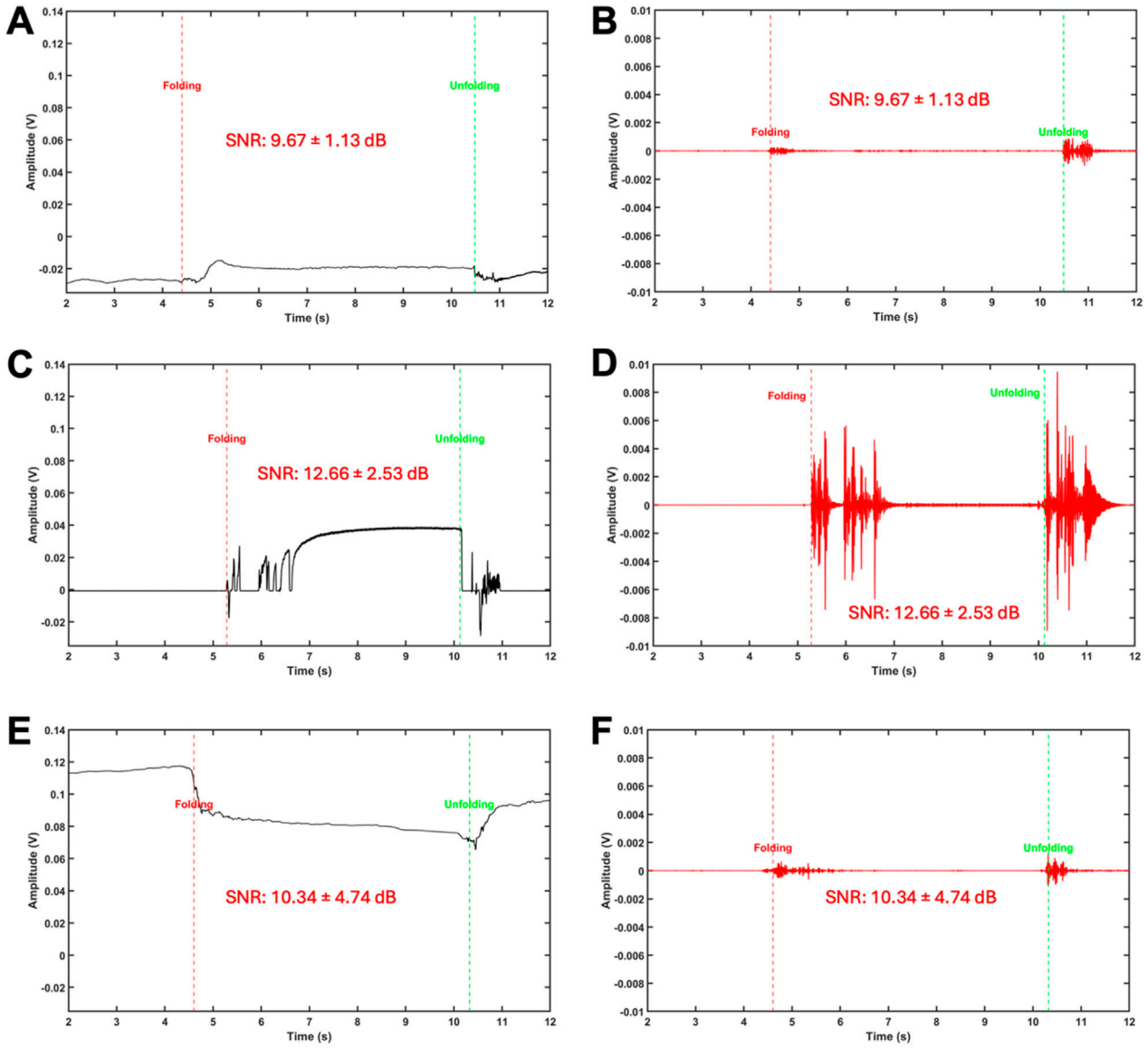

FIGURE 6
EMG signal recordings during folding motion for each electrode design. Panels **(A)**, **(C)**, and **(E)** show the raw signals captured using the open-mesh, closed-mesh, and island-bridge electrodes, respectively. Panels **(B)**, **(D)**, and **(F)** display the corresponding filtered signals for each design. Signal-to-noise ratio (SNR) values are included to quantitatively compare signal quality across the different electrode patterns.

gold and 0.1 Å/s for chromium and 100 W power for plasma initiation of both targets. The sputtering process utilized argon (Ar) gas to facilitate the deposition of the metal layers.

2.4 Laser cutting process

Laser cutting is a precise and controllable manufacturing technique for creating intricate patterns on flexible substrates and conductive layers. It is widely used to define conductive paths, insulating areas, and other microstructures in flexible electronics (Bian et al., 2019; You et al., 2020; Yu et al., 2023). A laser engraver can be effectively used to cut thin flexible electrodes, such as those made from polymer sheets like polyimides or Kapton, by carefully adjusting parameters such as laser power, cutting speed, and focus (Yan et al., 2022). The process involves attaching a polymer sheet, such as polyimide or Kapton, to a rigid support (e.g., a glass slide) and depositing a conductive metal layer (e.g., copper or silver). The desired electrode pattern is designed using CAD software and imported into the laser engraver's control software, where parameters like laser power and cutting speed are optimized for clean, precise cuts. After cutting, the patterned electrodes are transferred to a flexible substrate, such as polyurethane (PU), and encapsulated to ensure durability and insulation (Han et al., 2019; You et al., 2020; Akin et al., 2023; Dodd et al., 2023; Helgason et al., 2023; Wang et al., 2023). For example, Yan et al. used a fiber laser engraver to cut fine-pitch conductive traces on copper-Kapton substrates, selectively removing copper to create functional circuits. Another study demonstrated the use of a CO_2 laser to pattern laser-induced graphene (LIG) on polyimide, followed by

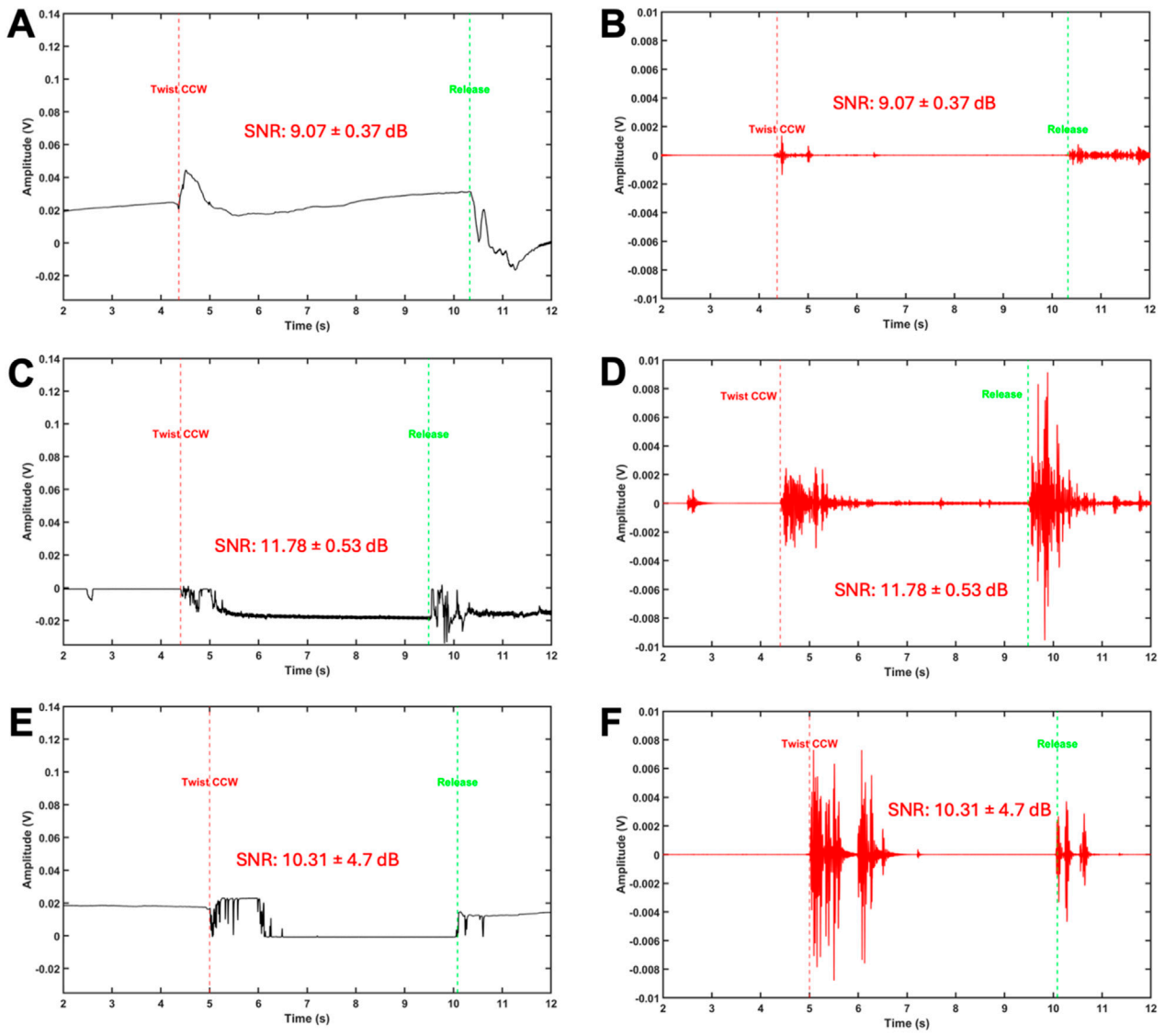

FIGURE 7
EMG signal data recorded during counterclockwise twisting motion using electrodes with different pattern designs: **(A)** raw signal from the open-mesh design, **(B)** corresponding filtered signal, **(C)** raw signal from the closed-mesh design, **(D)** corresponding filtered signal, **(E)** raw signal from the island-bridge design, and **(F)** corresponding filtered signal. Signal-to-noise ratio (SNR) values are also presented to evaluate the signal quality across the different electrode designs.

copper electroplating to enhance conductivity for high-resolution, flexible circuits (Babatain et al., 2025). Rodriguez et al. integrated aluminum nanoparticles into PET using a laser-driven process, creating highly conductive and robust circuits for applications like thermal heaters and sensors (Rodriguez et al., 2021).

In this study, 10 electrodes of each design were fabricated with a fixed-focus laser engraver (Sculpfun S9). This device produces a Class 4 laser with a maximum power of 5.5 W and a wavelength of 450 ± 5 nm. The laser engraver is shown in Supplementary Figure S1. The laser engraver was operated using the LaserGRBL software, which translates pattern designs into precise engraving or cutting actions. Several parameters in LaserGRBL influence the quality of the cutting process, including border speed, power, and B&W (Black & White) settings. The border speed controls the movement speed of the laser head during engraving or cutting along borders or outlines. A higher border speed reduces the risk of burning or overexposure at the edges, while a lower speed allows for deeper cuts but may cause excess heat buildup. The power setting, expressed as a percentage of the laser's maximum power, determines the intensity of the engraving or cutting. Higher power settings result in deeper cuts or stronger burns, whereas lower settings are better suited for delicate materials.

The B&W (Black & White) mode dictates how the laser interprets grayscale or colored images. For instance, a B&W threshold of 50 means that any pixel with a grayscale value above 50% (mid-gray) is treated as black (engraved at full power), while pixels below this threshold are treated as white (not engraved at all). To optimize the cutting process, a parametric study was conducted, varying the border speed from 150 to 1,000 mm/min, the power from 2% to 10%, and the B&W threshold from 40 to 90. The optimal parameters were determined to

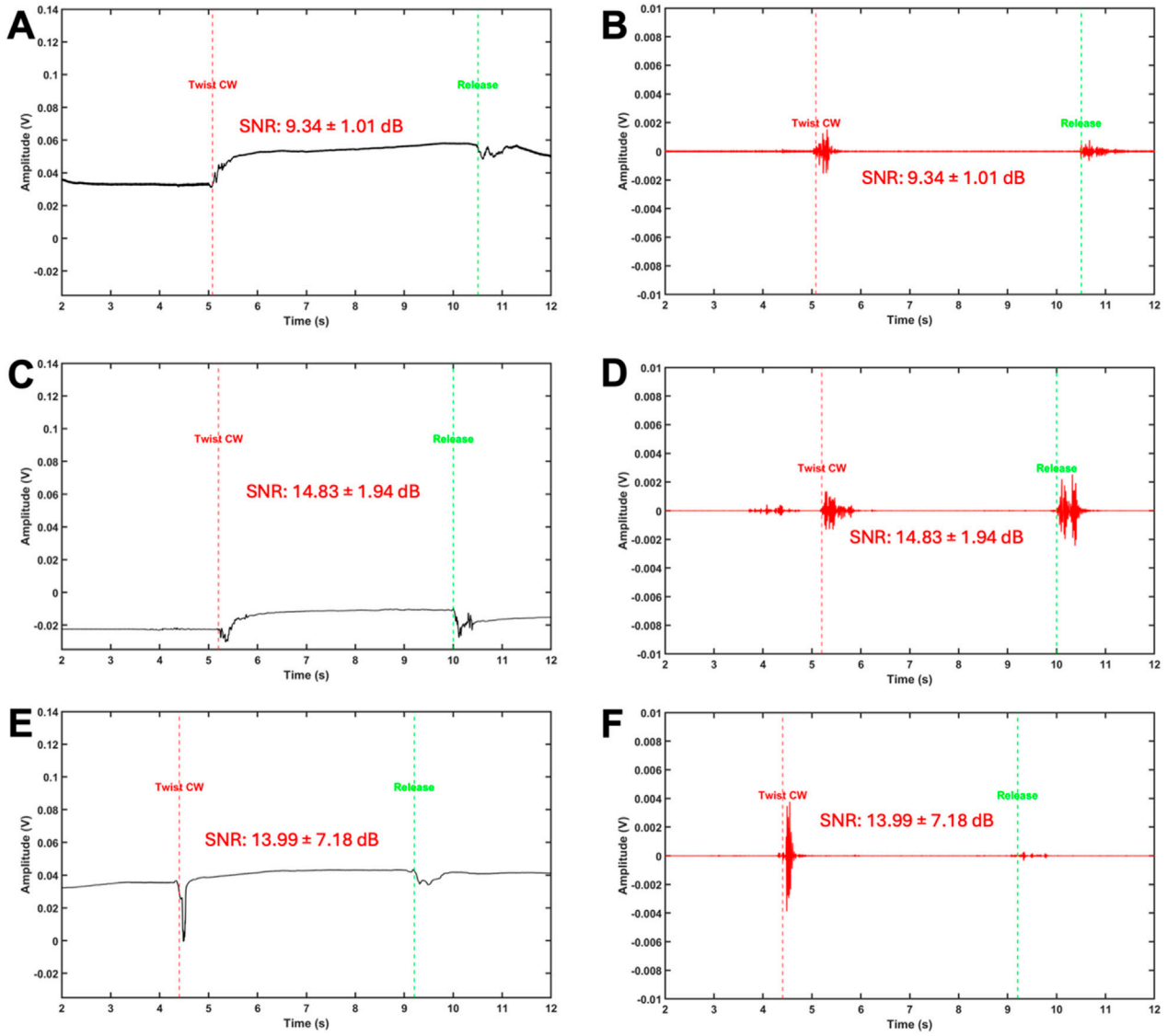

FIGURE 8
EMG signals recorded during clockwise twisting motion for the three electrode designs. Panels **(A)**, **(C)**, and **(E)** show raw EMG signals captured using the open-mesh, closed-mesh, and island-bridge electrodes, respectively, while panels **(B)**, **(D)**, and **(F)** display their corresponding filtered signals. Signal-to-noise ratio (SNR) values are included to quantitatively assess the signal quality and filtering effectiveness for each electrode configuration.

be 3% power, 150 mm/min border speed, and a B&W threshold of 50. Further details on the parametric study are provided in Supplementary Table S1.

To confirm fabrication consistency across samples, dimensional measurements of trace width and gap size were conducted on ten electrodes per design. As summarized in Supplementary Table S2, all three patterns exhibited minimal dimensional variation, with standard deviations within ±3% of their nominal values. This consistency highlights the high reproducibility and precision of the laser cutting process used in this study.

2.5 Electrode characterization

After cutting the serpentine, island, and network-shaped patterns, the gold-coated PI film outside the patterns was carefully peeled off. The patterned electrodes were then transferred onto pieces of 2-inch-wide water-soluble tape (3M Water Soluble Wave Solder Tape 5,414). Finally, the electrodes were transferred onto silicone tapes (YRVHCK Silicone Scar Tape) for further use.

The mechanical performance of the electrodes for each design was evaluated through bending and stretching tests. To assess their mechanical and electrical robustness, 100 bending cycles were performed at 90° and 180°, with electrical resistance measured at the four corners after each cycle. For the bending tests, the prepared flexible electrodes were attached to 90° and 180° guides that were pre-fabricated using 3D printing to ensure consistent and repeatable deformation. For the stretching tests, the electrodes were elongated to 10%, 20%, and 30% strains in both longitudinal and transverse directions, and the corresponding electrical resistance was recorded. A custom-built stretching apparatus was used for this test (shown in

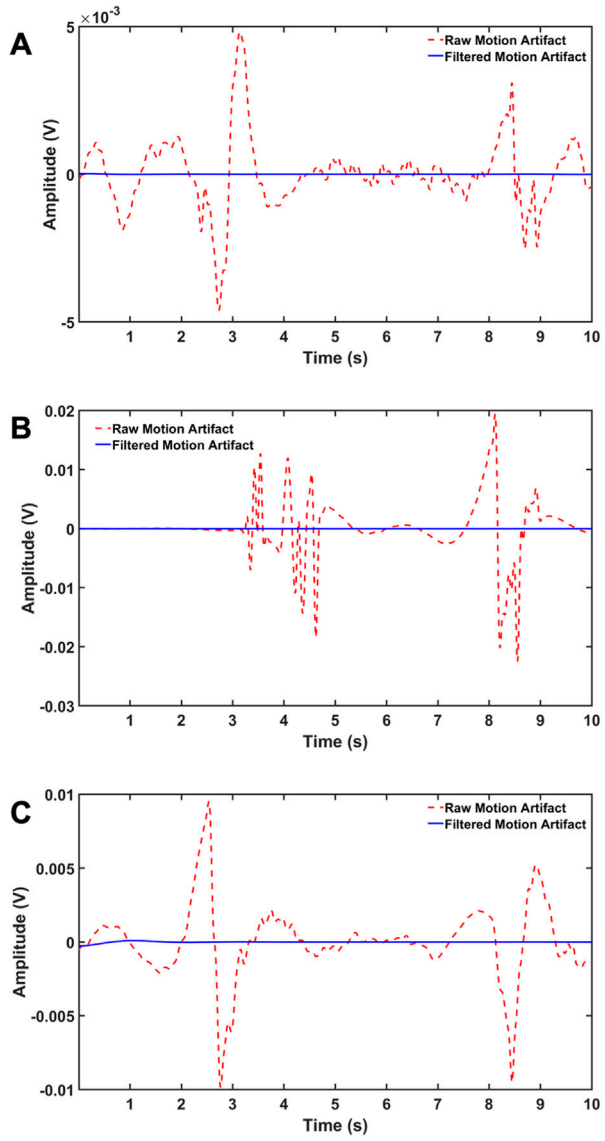

FIGURE 9
Time-domain motion artifact signals during folding–unfolding motion for the three electrode designs: **(A)** open-mesh, **(B)** closed-mesh, and **(C)** island-bridge. The raw motion artifact (0.5–10 Hz band, red dashed line) and the corresponding filtered signal (blue solid line) are overlaid. Significant attenuation of motion-induced low-frequency fluctuations is observed after filtering.

Supplementary Figures S2–S7), allowing the electrodes to be placed flat and gradually stretched by rotating a control knob. The resulting deformation was quantified using a slide caliper for accurate strain measurement. The detailed experimental setup is shown in Supplementary Figures S2–S8.

2.6 EMG demonstration

The prepared electrodes and a reference electrode were placed on the skin and connected to a custom measurement circuit, as shown in Figure 2A. The two measurement electrodes featured identical pattern designs (Figure 2B), while a commercial gel electrode (3M 2560–5, Red Dot Monitoring Electrode) served as the reference (Figure 2C). The reference electrode was placed on the ulnar styloid process of the left wrist, while two measurement electrodes were positioned 2 cm apart (center-to-center) on the flexor side of the forearm. Prior to electrode placement, the skin was prepared by cleansing with 70% isopropyl alcohol, allowing it to dry, and then gently abrading the site with a skin prep pad to reduce impedance. The electrodes were firmly applied to the prepped skin, with pressure applied around the edges to ensure optimal adhesion and signal contact.

The custom circuit (Figure 2D) included a Bluetooth Low Energy (BLE) chip, a 2.45 GHz chip antenna, and a rechargeable battery, with the functional architecture shown in Figure 2E (Kwon et al., 2020). EMG signals captured by the electrodes were amplified and filtered by analog circuitry, then digitized using an onboard analog-to-digital converter (ADC). The microcontroller processed the digital signals using embedded filtering and compression algorithms, after which the BLE module encoded and transmitted the data via the 2.45 GHz antenna. The signal was wirelessly received, displayed, and stored on a connected Android smartphone or tablet.

The same acquisition protocol was applied across all three electrode designs to ensure consistency. EMG recordings were conducted during two types of hand movements: folding (flexion and extension) and twisting (clockwise and counterclockwise). Each motion was repeated four times for 10 s with rest intervals between trials. The experimental setup for the folding motion is shown in Supplementary Figure S9.

2.7 Signal-to-noise ratio analysis

The EMG signal data underwent a series of filtering and analysis steps. To reduce noise, a 60 Hz notch filter was applied to eliminate powerline interference, followed by a 30–100 Hz bandpass Butterworth filter to isolate the EMG frequency range while removing low-frequency noise and high-frequency artifacts. Root Mean Square (RMS) analysis was performed on the filtered signal to evaluate its power, and a moving average was applied to smooth out fluctuations. Peaks in the RMS signal, representing significant muscle activity, were detected using a threshold set at 10% of the maximum RMS value. The average amplitude of these peaks is used as the signal level, while the mean of the entire smoothed RMS trace is treated as the noise level. The final SNR is computed in decibels using Equation 1.

$$\mathrm{SNR}_{\mathrm{dB}} = 20\log_{10}\left(\frac{\mathrm{Signal}}{\mathrm{Noise}}\right) \tag{1}$$

The average SNR of four measurements was used to compare the three designs under different types of motions.

To further validate filtering performance, short-time Fourier transform (STFT) analysis was performed. Supplementary Figures S10–S12 present time–frequency spectrograms of raw and filtered EMG signals during folding and twisting tasks. The raw signals display substantial low-frequency noise and 60 Hz interference, while the filtered signals show enhanced signal energy concentrated between 30 and 100 Hz. Supplementary Figures S13–S15 show

corresponding power spectral density (PSD) plots, confirming that high-frequency noise components are also suppressed post-filtering. Supplementary Table S3 summarizes the time-domain and STFT-based SNR values and the calculated SNR improvements for each design and motion type. Together, these analyses validate that the filtering pipeline effectively removes motion and environmental noise while preserving physiologically meaningful EMG content (Phinyomark et al., 2012; Rangayyan, 2015; Farina et al., 2025).

In addition to the SNR analysis, the sensor's susceptibility to motion artifacts was quantitatively evaluated using a time-domain approach that targets low-frequency components commonly associated with motion-induced disturbances. The raw EMG signals were bandpass-filtered between 0.5 and 10 Hz using a fourth-order Butterworth filter to isolate motion artifact contributions. The root-mean-square (RMS) amplitudes of these low-frequency components were computed from both raw and filtered signals to quantify artifact magnitude. A Motion Artifact Index (MAI) was then derived, reflecting both the absolute RMS value and the percentage of total signal energy attributable to motion artifacts. Additionally, the motion artifact suppression ratio was calculated in decibels to evaluate the effectiveness of the filtering strategy. This analysis provides an objective measure of artifact mitigation beyond signal fidelity alone (De Luca et al., 2010; Fratini et al., 2009; H, 2017; Usuga et al., 2022).

3 Results and discussion

3.1 Electrode pattern fabrication

The three electrode geometries—open-mesh, closed-mesh, and island-bridge—were successfully fabricated through laser cutting of gold-coated PI substrates. The patterning process followed the steps illustrated in Figures 3A–L. After cutting (Figures 3D–F), the electrodes were transferred to water-soluble tape (Figures 3G–I) and then to silicone tape (Figures 3J–L). These steps were performed consistently across all samples to ensure reproducibility and reliable geometry transfer.

3.2 Electromechanical performance under stretching

In our experiments, all three electrode designs maintained excellent electromechanical stability under uniaxial stretching up to 30% in both longitudinal and transverse directions, as shown in Figure 4. Resistance variation remained within ±7% across all conditions.

The open-mesh design exhibited the highest resistance variation, reaching ±6.2% in the longitudinal (Figure 4A) and ±4.7% in the transverse direction (Figure 4B). This outcome reflects the design's inherent mechanical flexibility but also its susceptibility to path distortion during deformation. This agrees with observations from (Hocheng and Chen, 2014), who reported that open structures can result in compromised electrical pathways under strain.

The closed-mesh design, by contrast, demonstrated the most stable resistance response, with variations limited to ±2.3% (Figure 4C) and ±1.21% (Figure 4D) in the longitudinal and transverse directions, respectively. Our results suggest that the compact and continuous mesh structure contributes to improved conductivity under strain, consistent with findings from (Li et al., 2024), who emphasized the importance of dense conductive networks for signal integrity.

The island-bridge design showed anisotropic behavior. It achieved the lowest resistance variation (±1.32%) under longitudinal strain (Figure 4E), while the transverse direction showed higher fluctuation (±2.56%, Figure 4F). This supports the idea that stress is isolated to the flexible bridges while the rigid islands preserve electrical functionality, as previously proposed by (Yang et al., 2022). Table 2 summarizes these findings numerically.

3.3 Resistance stability during bending cycles

To evaluate mechanical durability, we subjected all electrode designs to 100 bending cycles at 90° and 180°, recording resistance after every 10 cycles (Figure 5). Our results show a clear hierarchy in stability:

The open-mesh design had the highest variation (±6.86%, Figure 5A), attributed to fatigue accumulation at sharp bends and deformation of thin traces. The closed-mesh design showed a moderate variation of ±4.49% (Figure 5B), benefiting from its structural uniformity. The island-bridge design performed best, with only ±1.61% variation (Figure 5C), indicating strong durability due to mechanical decoupling. These findings align with previously reported concepts of structural decoupling improving mechanical resilience (Yang et al., 2022).

3.4 Real-time EMG signal performance

We assessed the functional performance of each electrode design by analyzing EMG signals recorded during dynamic hand movements (folding, clockwise twisting, and counterclockwise twisting). Signal fidelity was quantified using signal-to-noise ratio (SNR), summarized in Table 3 and Figures 6–8.

The closed-mesh electrodes delivered the highest SNR values across all motion types—12.66 ± 2.53 dB during folding (Figure 6D), 11.78 ± 0.53 dB during counterclockwise twisting (Figure 7D), and 14.83 ± 1.94 dB during clockwise twisting (Figure 8D). These consistent results confirm that the continuous, networked structure maintains stable skin contact and resists motion artifacts. This observation is consistent with prior studies on structured electrodes enhancing motion resistance (Cheng et al., 2023b; J. Wang et al., 2025).

In contrast, the open-mesh design exhibited lower overall SNR values—9.67 ± 1.13 dB (Figure 6B), 9.07 ± 0.37 dB (Figure 7B), and 9.34 ± 1.01 dB (Figure 8B)—but demonstrated remarkable consistency across trials. While its porous and highly flexible structure compromises electrode-skin contact under deformation, resulting in reduced signal strength, the low standard deviations reflect stable performance. This predictable behavior may be advantageous in scenarios where consistent signal quality is more critical than peak amplitude, particularly in repetitive or twisting motions, supported by prior studies (Cheng et al., 2023b; Kim et al., 2023; Wang et al., 2020).

The island-bridge electrodes achieved intermediate SNR values—10.34 ± 4.74 dB (Figure 6F), 10.31 ± 4.70 dB (Figure 7F),

and 13.99 ± 7.18 dB (Figure 8F)—but with high variability. This outcome reflects the hybrid architecture of the design: rigid islands provide high-quality signal contact points, while the flexible bridges are more susceptible to strain-induced inconsistencies. The elevated variability during clockwise twisting suggests that bridge deformation under certain motion patterns may intermittently disrupt conductive pathways, affecting signal reliability despite periods of strong performance (Li et al., 2024).

A commercial gel electrode was used as a reference for signal comparison; however, direct impedance matching between the gel and flexible electrodes was not performed. While the signal quality appeared comparable, we acknowledge this as a limitation of the current study. A more detailed impedance analysis will be considered in future work to further support performance comparisons (Ferrer et al., 2024; Xiang et al., 2025; Yamada and Honda, 2025).

3.5 Effect of motion type on signal quality

Across all designs, motion type significantly affected signal quality. Folding movements consistently produced lower SNRs due to localized skin compression and increased impedance fluctuations. In contrast, twisting motions, especially clockwise rotation, resulted in better performance for the closed-mesh and island-bridge designs. These trends support findings by (Li et al., 2024), which reported that distributed strain leads to better signal preservation than concentrated deformation.

3.6 Dynamic response to motion artifacts

Figure 9 shows time-domain motion artifact signals during folding–unfolding motion for the three electrode designs: (A) open-mesh, (B) closed-mesh, and (C) island-bridge. In each case, the raw signal (red dashed line) contains prominent low-frequency fluctuations (0.5–10 Hz), which are substantially attenuated after filtering (blue solid line). The closed-mesh design exhibits the highest artifact amplitude, while the island-bridge and open-mesh designs display moderate and lower levels, respectively. These results confirm the filtering pipeline's effectiveness in suppressing motion-induced disturbances. Quantitative metrics—including the Motion Artifact Index (MAI), RMS amplitudes before and after filtering, and suppression ratios—are summarized in Supplementary Table S4. Additional time-domain analyses for twisting motions are provided in Supplementary Figures S16–S17, further supporting the robustness of the filtering strategy.

4 Conclusion

This study systematically evaluates the mechanical durability and EMG signal quality of three flexible electrode designs—open-mesh, closed-mesh, and island-bridge—fabricated using a laser cutting technique on gold-coated PI substrates. Electromechanical performance and real-time EMG acquisition were assessed under controlled stretching and bending.

The open-mesh design exhibited the greatest mechanical flexibility, but significant electrical instability, with notable resistance fluctuations during stretching and bending, and relatively low EMG signal quality across motion types. The island-bridge design offered strong bending durability and low stretch-induced changes but showed inconsistent EMG performance, likely due to strain concentration at the bridge regions. The closed-mesh design demonstrated the most balanced performance, with stable resistance across mechanical tests and the highest, most consistent EMG signal quality. Its dense conductive network contributed to stable skin contact and minimal motion artifacts across all testing conditions.

These findings highlight the importance of electrode geometry in wearable bioelectronics. The closed-mesh configuration emerges as the most suitable for real-time, motion-intensive EMG applications, offering a favorable balance between mechanical stability and signal fidelity. Future work will explore hybrid geometries and encapsulation strategies to further optimize performance under complex deformations and extended use.

Data availability statement

The original contributions presented in the study are included in the article/Supplementary Material, further inquiries can be directed to the corresponding author.

Author contributions

AK: Data curation, Formal Analysis, Investigation, Methodology, Validation, Writing – original draft, Writing – review and editing. SB: Methodology, Writing – review and editing. W-HY: Conceptualization, Supervision, Writing – review and editing. J-HK: Conceptualization, Data curation, Formal Analysis, Funding acquisition, Investigation, Methodology, Project administration, Resources, Supervision, Validation, Writing – original draft, Writing – review and editing.

Funding

The author(s) declare that financial support was received for the research and/or publication of this article. Commercialization Gap Fund (GR00013451) from the Office of Commercialization at Washington State University.

Acknowledgments

J.-H.K acknowledges the support of the Commercialization Gap Fund provided by the Office of Commercialization at Washington State University. W.-H.Y. acknowledges the support of the WISH Center at the Institute for Matter and Systems at Georgia Tech.

Conflict of interest

The authors declare that the research was conducted in the absence of any commercial or financial relationships that could be construed as a potential conflict of interest.

The author(s) declared that they were an editorial board member of Frontiers, at the time of submission. This had no impact on the peer review process and the final decision.

Generative AI statement

The author(s) declare that no Generative AI was used in the creation of this manuscript.

Any alternative text (alt text) provided alongside figures in this article has been generated by Frontiers with the support of artificial intelligence and reasonable efforts have been made to ensure accuracy, including review by the authors wherever possible. If you identify any issues, please contact us.

Publisher's note

Supplementary material

The Supplementary Material for this article can be found online at: https://www.frontiersin.org/articles/10.3389/fnano.2025.1632279/full#supplementary-material

References

Abbas, A., Luo, Y., Ahmad, W., Mustaqeem, M., Kong, L., Chen, J., et al. (2024). Recent progress, challenges, and opportunities in 2D materials for flexible displays. *Nano Today* 56, 102256. doi:10.1016/j.nantod.2024.102256

Akin, S., Jo, S., and Jun, M. B.-G. (2023). A cold spray-based novel manufacturing route for flexible electronics. *J. Manuf. Process.* 86, 98–108. doi:10.1016/j.jmapro.2022.12.035

Babatain, W., Park, C., Ishii, H., and Gershenfeld, N. (2025). Laser-enabled fabrication of flexible printed electronics with integrated functional devices. *Adv. Sci.* 12, 2415272. doi:10.1002/advs.202415272

Bian, J., Zhou, L., Wan, X., Zhu, C., Yang, B., and Huang, Y. (2019). Laser transfer, printing, and assembly techniques for flexible electronics. *Adv. Electron. Mater.* 5, 1800900. doi:10.1002/aelm.201800900

Borók, A., Laboda, K., and Bonyár, A. (2021). PDMS bonding technologies for microfluidic applications: a review. *Biosensors* 11, 292. doi:10.3390/bios11080292

Cheng, L., Li, J., Guo, A., and Zhang, J. (2023a). Recent advances in flexible noninvasive electrodes for surface electromyography acquisition. *npj Flex. Electron.* 7, 39–26. doi:10.1038/s41528-023-00273-0

Cheng, L., Li, J., Guo, A., and Zhang, J. (2023b). Recent advances in flexible noninvasive electrodes for surface electromyography acquisition. *npj Flex. Electron.* 7, 39. doi:10.1038/s41528-023-0073-0

De Luca, C. J., Donald Gilmore, L., Kuznetsov, M., and Roy, S. H. (2010). Filtering the surface EMG signal: movement artifact and baseline noise contamination. *J. Biomech.* 43, 1573–1579. doi:10.1016/j.jbiomech.2010.01.027

Dodd, N., Ballantyne, E., Heron, G., and Goodall, R. (2023). Multi-layer laser cutting of electrical steel sheets applied to electric machine laminations. *PLoS One* 18, e0288232. doi:10.1371/journal.pone.0288232

Eyvazi Hesar, M., Khan, D., Seyedsadrkhani, N. S., and Ingebrandt, S. (2021a). Contactless, battery-free, and stretchable wearable for continuous recording of seismocardiograms. *ACS Appl. Electron. Mater.* 3, 11–20. doi:10.1021/acsaem.0c00768

Eyvazi Hesar, M., Khan, D., Seyedsadrkhani, N. S., and Ingebrandt, S. (2021b). Contactless, battery-free, and stretchable wearable for continuous recording of seismocardiograms. *ACS Appl. Electron. Mater.* 3, 11–20. doi:10.1021/acsaelm.0c00768

Farina, D., Merletti, R., and Enoka, R. M. (2025). The extraction of neural strategies from the surface EMG: 2004–2024. *J. Appl. Physiol.* 138, 121–135. doi:10.1152/japplphysiol.00453.2024

Ferrer, M. B., Harada, D., Martin, C. J., Métivier, R., Allain, C., Nakatani, K., et al. (2024). Cascade fluorescence modulation in photochromic microcapsules. *ACS Appl. Mater. Interfaces* 16, 57626–57635. doi:10.1021/acsami.4c09023

Fratini, A., Cesarelli, M., Bifulco, P., and Romano, M. (2009). Relevance of motion artifact in electromyography recordings during vibration treatment. *J. Electromyogr. Kinesiol.* 19, 710–718. doi:10.1016/j.jelekin.2008.04.005

H, A. V. (2017). A review on noises in EMG signal and its removal. *Int. J. Sci. Res. Publ.* 7, 23. Available online at: www.ijsrp.org.

Han, T., Nag, A., Afsarimanesh, N., Mukhopadhyay, S. C., Kundu, S., and Xu, Y. (2019). Laser-Assisted printed flexible sensors: a review. *Sensors* 19, 1462. doi:10.3390/s19061462

Helgason, R., Fathy, J., and Lai, Y. (2023). The effect of laser cutting on the Young's modulus of polydimethylsiloxane. *J. Micromanufacturing* 6, 60–65. doi:10.1177/25165984221131400

Hocheng, H., and Chen, C.-M. (2014). Design, fabrication and failure analysis of stretchable electrical routings. *Sensors* 14, 11855–11877. doi:10.3390/s140711855

Jiang, B., White, A., Ou, W., Van Belleghem, S., Stewart, S., Shamul, J. G., et al. (2022). Noncovalent reversible binding-enabled facile fabrication of leak-free PDMS microfluidic devices without plasma treatment for convenient cell loading and retrieval. *Bioact. Mater.* 16, 346–358. doi:10.1016/j.bioactmat.2022.02.031

Kim, G.-M., Lee, S.-J., and Kim, C.-L. (2021). Assessment of the physical, mechanical, and tribological properties of PDMS thin films based on different curing conditions. *Mater. (Basel)* 14, 4489. doi:10.3390/ma14164489

Kim, M., Kim, S., Kwon, Y. W., Seo, H., Chung, W. G., Kim, E., et al. (2023). Emerging bio-interfacing wearable devices for signal monitoring: overview of the mechanisms and diverse sensor designs to target distinct physiological bio-parameters. *Adv. Sens. Res.* 2, 2200049–28. doi:10.1002/adsr.202200049

Kwon, Y.-T., Kim, Y.-S., Kwon, S., Mahmood, M., Lim, H.-R., Park, S.-W., et al. (2020). All-printed nanomembrane wireless bioelectronics using a biocompatible solderable graphene for multimodal human-machine interfaces. *Nat. Commun.* 11, 3450. doi:10.1038/s41467-020-17288-0

Lee, H.-K., Chang, S.-I., and Yoon, E. (2006). A flexible polymer tactile sensor: fabrication and modular expandability for large area deployment. *J. Microelectromechanical Syst.* 15, 1681–1686. doi:10.1109/JMEMS.2006.886021

Lee, W. H., Cha, G. D., and Kim, D.-H. (2021). Flexible and biodegradable electronic implants for diagnosis and treatment of brain diseases. *Curr. Opin. Biotechnol.* 72, 13–21. doi:10.1016/j.copbio.2021.07.027

Li, R.-W., and Liu, G. (2019). *Flexible and stretchable electronics* (New York: Jenny Stanford Publishing). doi:10.1201/9780429058905

Li, K., Shuai, Y., Cheng, X., Luan, H., Liu, S., Yang, C., et al. (2022). Island effect in stretchable inorganic electronics. *Small* 18, 2107879. doi:10.1002/smll.202107879

Li, D., Cui, T., Xu, Z., Xu, S., Dong, Z., Tao, L., et al. (2024). Designs and applications for the Multimodal flexible hybrid epidermal electronic systems. *Research* 7, 0424–23. doi:10.34133/research.0424

Pan, T., Pharr, M., Ma, Y., Ning, R., Yan, Z., Xu, R., et al. (2017). Experimental and theoretical studies of serpentine interconnects on ultrathin elastomers for stretchable electronics. *Adv. Funct. Mater.* 27, 1702589–8. doi:10.1002/adfm.201702589

Park, S., Ban, S., Zavanelli, N., Bunn, A. E., Kwon, S., Lim, H., et al. (2023). Fully screen-printed PI/PEG blends enabled patternable electrodes for scalable manufacturing of Skin-Conformal, stretchable, wearable electronics. *ACS Appl. Mater. Interfaces* 15, 2092–2103. doi:10.1021/acsami.2c17653

Phinyomark, A., Nuidod, A., Phukpattaranont, P., and Limsakul, C. (2012). Feature extraction and reduction of wavelet transform coefficients for EMG pattern classification. *Electron. Electr. Eng.* 122. doi:10.5755/j01.eee.122.6.1816

Rangayyan, R. M. (2015). *Biomedical signal analysis* (Wiley). doi:10.1002/9781119068129

Rodriguez, R. D., Shchadenko, S., Murastov, G., Lipovka, A., Fatkullin, M., Petrov, I., et al. (2021). Ultra-Robust flexible electronics by Laser-Driven polymer-nanomaterials integration. *Adv. Funct. Mater.* 31, 2008818. doi:10.1002/adfm.202008818

Sakamoto, K., Kuwae, H., Kobayashi, N., Nobori, A., Shoji, S., and Mizuno, J. (2018). Highly flexible transparent electrodes based on mesh-patterned rigid indium tin oxide. *Sci. Rep.* 8, 2825. doi:10.1038/s41598-018-20978-x

Schneider, M., Möhwald, H., and Akari, S. (2003). Quantitative measurement of chromium's ability to promote adhesion. *J. Adhes.* 79, 597–607. doi:10.1080/00218460309539

Shamsiah Mohamed, N., and Ching Theng, K. (2019). Mechanical properties of graded polydimethylsiloxane for flexible electronics. *J. Phys. Conf. Ser.* 1150, 012030. doi:10.1088/1742-6596/1150/1/012030

Silva, C. A., lv, J., Yin, L., Jeerapan, I., Innocenzi, G., Soto, F., et al. (2020). Liquid metal based island-bridge architectures for all printed stretchable electrochemical devices. *Adv. Funct. Mater.* 30, 2002041–10. doi:10.1002/adfm.202002041

Todeschini, M., Bastos da Silva Fanta, A., Jensen, F., Wagner, J. B., and Han, A. (2017). Influence of Ti and Cr Adhesion Layers on Ultrathin Au Films. *ACS Appl. Mater. Interfaces* 9, 37374–37385. doi:10.1021/acsami.7b10136

Usuga, F. A. C., Gissel, C., and Hernández, A. M. (2022). Motion artifact reduction in electrocardiogram signals through a redundant denoising independent component analysis method for wearable health care monitoring systems: algorithm development and validation. *JMIR Med. Inform.* 10, 1–17. doi:10.2196/40826

Wang, Y., Yin, L., Bai, Y., Liu, S., Wang, L., Zhou, Y., et al. (2020). Electrically compensated, tattoo-like electrodes for epidermal electrophysiology at scale. *Sci. Adv.* 6, eabd0996. doi:10.1126/sciadv.abd0996

Wang, F., Liu, Q., Xia, J., Huang, M., Wang, X., Dai, W., et al. (2023). Laser lift-off technologies for ultra-thin emerging electronics: mechanisms, applications, and progress. *Adv. Mater. Technol.* 8, 2201186. doi:10.1002/admt.202201186

Wang, J., Li, X., Chen, H., Jiang, J., Huang, J., Lu, J., et al. (2025). A stretchable, permeable, and biocompatible fiber-reinforced hybrid hydrogel electrode for highly stable electrophysiological signal recording. *J. Mater. Chem. A* 13, 19325–19337. doi:10.1039/d4ta08229j

Wen, W., and Fang, F. (2022). Flexible sensors in smart textiles and their applications. *Wearable Technol.* 2, 83. doi:10.54517/wt.v2i2.1651

Xiang, Y, Zhang, B., Zhang, C., Zhu, H., Zhang, Q., and Zhu, S. (2025). Force-indicating smart adhesives enabled by mechanochromic elastomer. *Chem. Eng. J.* 508, 160875. doi:10.1016/j.cej.2025.160875

Xu, J., Li, Y., Liu, H., Wang, J., Wang, J., Hou, Q., et al. (2023). Integration of patterned electrolyte film and sacrificial substrate serpentine electrode of low curvature for high stretch supercapacitor, physiological signal detection. *Chem. Eng. J.* 472, 144907. doi:10.1016/j.cej.2023.144907

Yamada, S., and Honda, T. (2025). Development of supramolecular ionic gels with self-healing capability and biodegradability using a bioderived ionic liquid and poly(vinyl alcohol). *Nanoscale* 17, 2184–2192. doi:10.1039/D4NR04792C

Yan, Z., Sathya, A., Yusuf, S., Lien, J.-M., and Peng, H. (2022). "Fibercuit: prototyping high-resolution flexible and Kirigami circuits with a fiber laser engraver," in *Proceedings of the 35th annual ACM symposium on user interface software and technology* (New York, NY, USA: ACM), 1–13. doi:10.1145/3526113.3545652

Yang, J. C., Lee, S., Ma, B. S., Kim, J., Song, M., Kim, S. Y., et al. (2022). Geometrically engineered rigid island array for stretchable electronics capable of withstanding various deformation modes. *Sci. Adv.* 8, eabn3863. doi:10.1126/sciadv.abn3863

Yin, L., Lv, J., and Wang, J. (2020). Structural innovations in printed, flexible, and stretchable electronics. *Adv. Mater. Technol.* 5, 2000694–18. doi:10.1002/admt.202000694

You, R., Liu, Y., Hao, Y., Han, D., Zhang, Y., and You, Z. (2020). Laser fabrication of graphene-based flexible electronics. *Adv. Mater.* 32, 1901981. doi:10.1002/adma.201901981

Yu, H., Gai, M., Liu, L., Chen, F., Bian, J., and Huang, Y. (2023). Laser-induced direct graphene patterning: from formation mechanism to flexible applications. *Soft Sci.* 3. doi:10.20517/ss.2022.26